Appl. Phys. B 90, 383–390 (2008)
DOI: 10.1007/s00340-007-2914-1

Applied Physics B
Lasers and Optics

L. GUYON[1]
K.M. HAJEK[1]
F. COURVOISIER[1,3]
V. BOUTOU[1,✉]
R. NUTER[2]
A. VINÇOTTE[2,*]
S. CHAMPEAUX[2]
L. BERGÉ[2]
J.-P. WOLF[1,3]

Control of lasing filament arrays in nonlinear liquid media

[1] LASIM (UMR5579), Université Claude Bernard Lyon 1, 43 bd du 11 Novembre, 69622 Villeurbanne Cedex, France
[2] Département de Physique Théorique et Appliquée, CEA-DAM/Ile de France, B.P. 12, 91680 Bruyères-le-Châtel, France
[3] Université de Genève, 20 Rue de l'Ecole de Médecine, 1211 Genève 4, Switzerland

Received: 27 September 2007/
Revised version: 5 December 2007
Published online: 24 January 2008 •

ABSTRACT Multiple filamentation in a high concentration solution of coumarin 153 in ethanol is studied. It is shown that the output filament pattern may be controlled by placing diffractive elements (circular aperture, edge) in the input beam path. These filaments are formed in highly reproducible arrays along diffraction maxima corresponding to the element used. Experimental results are supported by numerical simulations. They confirm that diffraction-induced intensity gradients swamp modulational instability on the wavefront, forcing filaments to form along diffraction maxima. The effect of two-photon absorption by coumarin molecules on filament patterns is also investigated over a range of dye concentrations. Control results are finally exploited in the production of arrays of localized lasing filaments, which should open novel applications. The resultant lasing sources are mutually coherent and highly repeatable from shot-to-shot, as is shown by their far-field interference patterns.

PACS 42.65.Tg; 52.38.Hb; 42.68.Ay

1 Introduction

The propagation of high-intensity, ultra-short laser pulses through transparent media gives rise to two major nonlinear effects, namely the Kerr effect and electron plasma creation. These effects occur in competition, and under certain conditions, they may exist in dynamic equilibrium (see review papers [1–3]). In particular, when the laser input power is greater than the initial power for self-focusing, P_{cr}, spatial compression of the beam takes place, which is saturated by plasma generation. The beam then becomes self-guided and is known as a "filament". Employing even higher powers promotes the formation of multiple filaments across the wavefront. Interest centers around two fundamental issues: firstly, the mechanisms involved in multiple filament formation, and secondly, the influence of competing effects (such as the Kerr effect, plasma defocusing, inter-filament interaction, etc.) on their propagation. Classic explanations invoke modulational instability theory to explain filament formation [4–6]. In this process, local intensity inhomogeneities on a plane-wave envelope grow exponentially and produce several small-scale cells conveying each a few critical powers for self-focusing across the beam [6, 7]. From this reasoning, it follows that the filament pattern at the exit of the nonlinear medium should be random and vary considerably from shot-to-shot, just as the instigating noise in the wavefront is random. This result has in fact been observed where the incident beam undergoes free propagation prior to entering a region with strong nonlinearities [8]. In contrast, the insertion of various optical elements in the beam path is seen to result in reproducible filamentation patterns [8–13], leading to the conclusion that there exist other effects which swamp modulational instability in multifilament formation. Reference [12] showed beam ellipticity to be one such effect, independent of medium and pulse duration. The role of ellipticity in shot-to-shot stability was confirmed in [11], among others. This tends to involve phase modulation of the input beam through, for example, the insertion of a tilted lens into the incident beam path [13]. A second manner of inducing stable filament patterns is to modify the incoming beam's intensity profile, leading to filament formation from sharp intensity gradients. According to [13], a mask as simple as a circular diaphragm can fulfill this objective. More extensive control may be achieved with two-dimensional arrays, such as a wire mesh [8, 9], or an array of diffractive microlenses [14]. Leaving to one side the question of active fluence pattern control, as demonstrated by [15], we confirm the role of passive optical elements in multiple filament formation from femtosecond pulses in condensed media, extending work published in [16]. The nonlinear media considered are ethanol and a solution of fluorescent dye coumarin in ethanol. While only one input beam geometry was considered in [16], fluence patterns at the output of the media are now compared for several geometries, including free propagation, a circular aperture, and a sharp edge. The patterns produced are seen to be extremely repeatable over a large number of laser shots, as well as organized into lattice-like arrangements. Further details of this process are examined by means of direct numerical simulations, which are in close agreement with our experimental results. Preliminary simulations were discussed in [16] in an investigation of fil-

✉ Fax: +33 472445871, E-mail: boutou@lasim.univ-lyon1.fr
*_Permanent address_: Glaizer Group, 15 rue Jean Jaurès, 92260 Fontenay-aux-Roses, France

ament propagation, to which additional experimental results are here added. Filament propagation has been studied extensively in various media. For instance, such nonlinear structures are currently exploited in a wide range of remote sensing applications [17]. Matters are not so clear in the domain of condensed media due to the potential augmentation of effects competing with Kerr focusing. In particular, dispersion, which is rather weak in air [18], and multi-photon absorption are important in such media, besides plasma defocusing. Several studies have, in fact, indicated that material dispersion can dominate over plasma self-channeling [18, 19]. Following computational studies, as well as experiments visualizing the filamentation process using weak fluorescent dye solutions (e.g., methanol) [19–21], the role of the low-intensity peripheral region in maintaining the intense filament core is recognized to be crucial. Despite few theoretical investigations [22], the role of nonlinear absorption losses, however, has not as yet been fully resolved, with a scarcity of experimental studies in particular. Where multi-photon excitation of dye molecules has been exploited for visualization purposes, the dye concentration was sufficiently weak to neglect absorption losses [21]. In contrast, this paper examines the effect of high dye concentrations (leading to between 10% and 35% absorption losses) on filament propagation. Several concentrations of the fluorescent dye coumarin 153 in ethanol are compared with filaments in pure ethanol, with particular emphasis on filament numbers and characteristics. This extends our previous work [16] and supports the general scope of studying filamentation in dye-diluted liquids, also used for amplification [23]. Finally, we combine our results on the control of multifilament patterns with the strong two-photon absorption (TPA) observed in the coumarin solution to generate organized arrays of micron-sized lasing sources. Several dyes have long been exploited as single-photon gain media, while multi-photon pumping only became accessible with the advent of high power lasers. The feasibility of this process was shown by He et al., pumping coumarin 500 with an 800 nm nanosecond pulse to produce a resultant ns-length and mm-size beam at around 479 nm [24]. More efficient multi-photon pumping can be achieved in the high-intensity conditions existing in femtosecond filaments in both gas [25, 26] and condensed media [27]. In air, amplified spontaneous emission (ASE) from N_2 and N_2^+ was observed in the backscattered fluorescence from a single filament [25]. While the above involve many photons, two-photon pumping is more common in condensed media. For instance, stimulated emission at 334 nm (in a solution of rhodamine-6G in methanol) was pumped in a TPA process by a femtosecond pulse and seeded by the resultant supercontinuum [27]. In contrast to this seeding process, which is very sensitive to the relative positions of the nonlinear medium and focal point, we previously demonstrated the generation of lasing sources in coumarin 153 in a pump-dump configuration [16]. This was the first example of multiple localized beams generated from multiple filaments. The highly localized distribution of high intensity in multifilament patterns means that TPA (for the creation of gain) is much more efficient at the filament sites. Hence, by subsequently adding a dump pulse, we are able to generate an array of laser sources from a single input pulse. Their organized arrangement and around 10 microns spot size make the development of such laser sources highly desirable for applications such as parallel information storage and processing [28]. Here, we extend our previous results to implement passive control of the output lasing arrays. The paper is organized as follows. Our experimental setup is presented in Sect. 2, while Sect. 3 discusses the control of multifilament patterns by altering the input beam's spatial profile. Both experimental and numerical results are presented in this section. Section 4 treats the effect of dye concentration on filament distribution and characteristics. Finally, the creation of micrometric lasing sources on filament sites is developed in Sect. 5.

2 Experimental setup

The experimental setup, displayed schematically in Figs. 1 and 2, involves 120–150 fs, 810 nm pulses delivered by an amplified mode-locked Ti:sapphire oscillator entering a standard pump-dump arrangement. The incoming femtosecond pulse has a maximum energy of a few millijoules and a 20 Hz repetition rate, with 30% of the energy diverted into the "dump" arm. In this arm, the beam is first focused into a 1 mm thick sapphire slab, so as to generate a supercontinuum. A series of filters then select the desired dump wavelength, i.e., 530 ± 10 nm, corresponding to the peak emission wavelength of coumarin 153. The two pulses, pump and

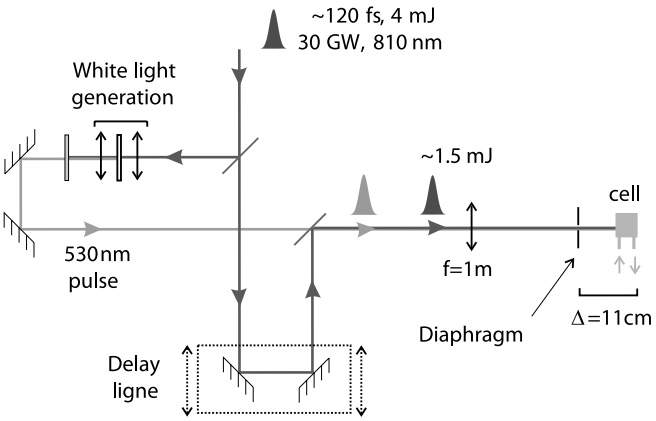

FIGURE 1 Schematic diagram of experimental pump-dump configuration

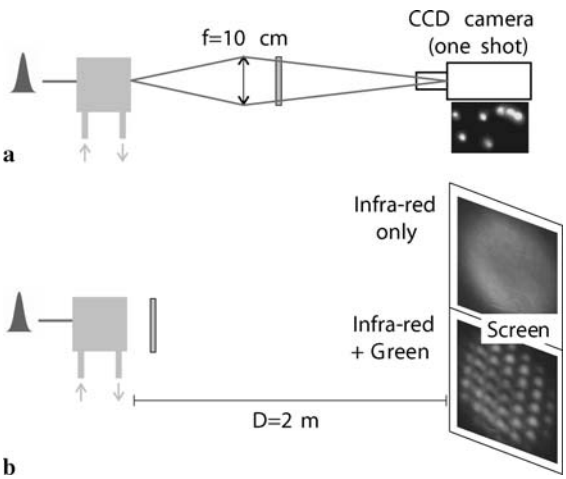

FIGURE 2 Schematic diagram, with sample results, of setup for imaging: (**a**) cell output fluence pattern; (**b**) far-field interference pattern

dump, are recombined in a beamsplitter and pass through a 1 m-focal-length lens before impinging on a 1 cm-long cuvette containing the nonlinear medium. A delay line in the pump arm ensures that the dump pulse arrives after the pump at the cell. The dump pulse intensity at this point does not exceed 10^5 W/cm^2, while that of the pump pulse is typically 4×10^{11} W/cm^2. This intensity is sufficient to induce multifilamentation in the nonlinear medium.

We first investigate passive control of filamentation patterns by placing a circular aperture or a slit a few centimeters in front of the cuvette. To achieve clearer filamentation patterns, we focus the input beam on one of the sharp edges of the slit so that the relevant diffracting element is thus a sharp edge, and not a slit. A CCD camera, coupled with an appropriate neutral density filter and a focusing lens, is used to image the cuvette output plane and is synchronized so as to capture single-shot fluence patterns (Fig. 2a). In this configuration, the dump arm of the optical setup is blocked. This configuration is maintained for the second set of experiments, with the exception that a circular aperture of fixed diameter (1 mm diameter) is always left in place. We study the influence of nonlinear losses on the multifilamentation process by varying the concentration of coumarin (up to 4 g/l) in the cell. Coumarin 153 in ethanol was chosen for its accessible absorption band, easily reached by two 810 nm photons. Both arms of the optical setup are employed for the experiments on lasing sources. As well as the output fluence, we image the cell's far-field interference pattern with a Nikon D70 reflex camera on a screen 2 m distant from the cell (Fig. 2b). Furthermore, we filter out the pump wavelength, only recording the pattern resulting from 530 nm (the dump wavelength) fluorescence or stimulated emission. The typical exposure time varies between 5 and 30 s, corresponding to integration over hundreds of laser shots. The regularity and contrast of the far-field interference patterns are used as indicators of the regularity and coherence of our filament-generated lasing sources.

3 Filament pattern control

3.1 *Experimental results*

To study the role of passive diffractive elements in controlling multifilament arrays, we compare the propagation of femtosecond pulse through three classes of elements, namely, no element, circular apertures and sharp edges, inserted in the beam path. For each type of element, a typical fluence pattern at the output plane of the nonlinear medium is shown in Fig. 3, in which filaments appear as individual bright zones. From a comparison of Fig. 3a and b, it is evident that the number of filaments is greater in the presence of a diffractive element (aperture) than in the free propagation case. This feature is also observed when coumarin is added into the ethanol cell (Fig. 3c).

Furthermore, filaments are primarily localized along annular rings (sections of annular rings are pointed out at the top of Fig. 3b) or vertical "stripes" (Fig. 3c) when the beam traverses an aperture or an edge, respectively, compared to the random arrangement resulting from free propagation. These filament patterns may easily be recognized as mirroring diffraction maxima corresponding to the pertinent element. In the case of the sharp edge, for example, if overall beam divergence is neglected, Fresnel diffraction theory can be used to estimate the distance between adjacent diffraction peaks. Substituting $\lambda_0 = 810$ nm (the laser wavelength) and $\Delta = 11$ cm (the distance between the diffractive element and cell output plane, see Fig. 1) into $\sqrt{\lambda_0 \Delta}$ yields a distance of approximately 300 μm. This order of magnitude is in agreement with the experimental observation of a distance of about 200 μm between the two vertical stripes of Fig. 3c. Hence, when the beam is sharply "cut" in space, the resultant intensity gradients (here, at the edges of the beam) force the formation of multiple filaments in these regions. This confirms the results presented in, for example, [9, 13]: steep gradients along diffraction maxima are amplified by the Kerr effect, increasing the local intensity and intensity gradient in that region, and thus creating the conditions necessary for filament formation. This reasoning also explains the relative paucity of filaments towards the center of the field, relative to the bright rings or stripes. The greatest intensity gradients occur close to the sharp edges of the diffractive element, with gradients diminishing towards the center. Filaments are therefore slower to form in this region, despite comparable overall intensity. The breakup of annular rings into individual filaments (Fig. 3b) results from azimuthal modulational instability [6, 29]. It should be noted that both sufficient intensity gradients (for modulational instability) and intensity (i.e., critical intensity) are required to trigger filament formation. As our input beam's spatial profile is far from uniform (Gaussian), there is insufficient intensity in certain portions of the wavefront for filaments to form, despite the sharp intensity gradients imposed by diffraction. This explains the 'patchy' nature of patterns in Fig. 3, especially in Fig. 3b, where only one section of the diffraction ring contains many filaments. A second important feature revealed by Fig. 3 is that, not only can the output fluence pattern be controlled through the use of passive diffractive elements, but the distance between filaments is also approximately constant. For the circular aperture, the inter-filament distance is around 50 μm, which matches the range measured for the sharp edge, namely 55 ± 7 μm. This value was obtained by taking the average of the inter-filament distance over the eight filaments labelled on the inner right "stripe" in

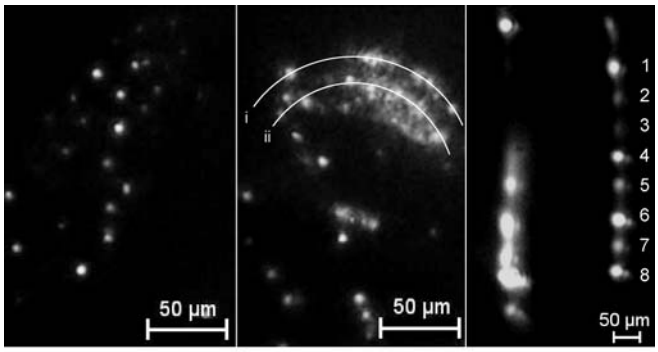

FIGURE 3 Typical experimental fluence patterns at the output plane for propagation through a 1 cm cell filled with (**a**, **b**) ethanol or (**c**) $C = 4$ g/l coumarin 153 in ethanol. Comparison of the effect of various diffractive elements: (**a**) no diffractive element, (**b**) circular aperture and (**c**) sharp edge. In case (**b**), sections of two concentric circles are superimposed to the filaments pattern in order to emphasize the position of the diffracted annular rings. In case (**c**), filaments are labelled from 1 to 8 in order to point out the inter-distance filament

Fig. 3c. Both experimental figures are also supported by that obtained from modulational instability theory. At a given critical power and input intensity I_0, the inter-filament distance, in the limit of weak dissipation, scales as $\lambda_{MI} \simeq \sqrt{\pi P_{\rm cr}/I_0}$, where $P_{\rm cr} = \lambda_0^2/2\pi n_0 n_2$ depends on the laser wavelength λ_0 and the linear ($n_0 = 1.36$) and nonlinear (n_2) indices of refraction [1, 4, 5, 30]. Taking $n_2 = 2.6 \times 10^{-16}\,{\rm cm}^2/{\rm W}$ for pure ethanol [16], we find that the distance computed using our input intensity of $I_0 = 4 \times 10^{11}\,{\rm W/cm}^2$ is about 48 μm, consistent with our experimental observations. Added to this equidistance between filaments is their great positional stability, illustrated by two single-shot images in Fig. 4. Both single-shot images are part of the double annular rings formed from diffraction through an aperture, and are separated by a time interval of a few seconds. Filament stability is made even clearer by the stability of far-field interference patterns (as will be discussed in the section on lasing filaments); these remained constant over exposures of around 30 s in duration, comprising more than 200 laser shots. It may be noted in Fig. 4 that the relative intensity of filaments varies between shots, some switching 'on' and others 'off', depending on the intensity available. These fluctuations are of second-order. They depend on the available energy and on local variations in the input beam's temporal and spatial profile. Nonetheless, our three results of forced pattern, equidistant filaments, and extremely reproducible filament pattern confirm the suitability of controlling multiple filament arrays with passive diffractive elements.

As for the remarkable positional stability and constant inter-filament distance, Dubietis et al. [19] explain such features with reference to the low-intensity radiation reservoir surrounding a filament. In essence, this reservoir feeds its energy into the filament as it propagates, which leads to the requirement for a minimum radius reservoir around each filament and thus to a minimum inter-filament distance. Where diffracting elements force filaments to form first in reproducible regions (the high-intensity-gradient diffraction maxima), this additional condition on inter-filament distance results in the high stability observed here. Comparable properties were reported for atmospheric propagation in the seminal papers by Moloney and co-workers [31, 32]. In the following sections, these results are compared to numerical simulations, in order to elucidate further details of this control process.

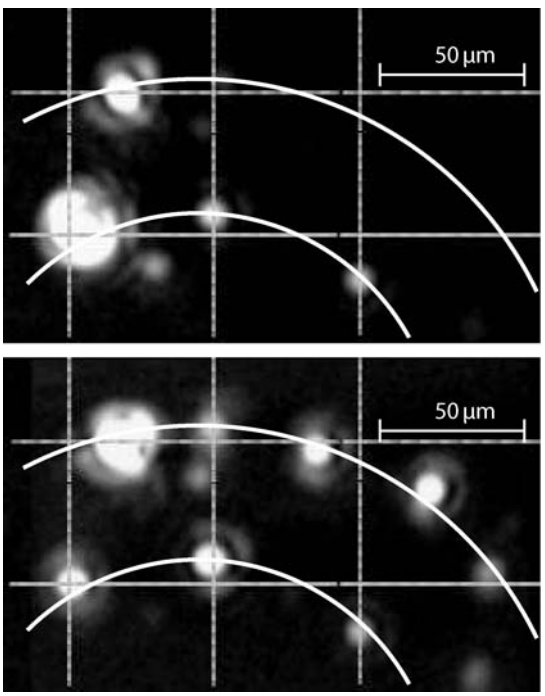

FIGURE 4 Stability of filament patterns along double annular rings (materialised by two sections of circles) formed by propagation through circular aperture. Each *image* corresponds to a single laser shot. *Images* are separated in time by a few seconds. The additional grid is drawn to emphasize the positional stability of each filament in the pattern. Note that the *grey scale* for the intensity is linear

3.2 *Numerical simulations*

We use a $(3+1)$-dimensional numerical model to simulate the cell output fluences for different input configurations (aperture, slit, etc.). In [16], we showed qualitative agreement between multifilament fluence patterns generated in ethanol and in the coumarin solution. The presence of additional terms, especially TPA, makes modeling the dye solution prohibitively time-consuming. Furthermore, the question addressed here is the role of the input beam shape in the filamentation pattern, which is comparable in both types of liquids. Therefore, we simulate only the pure ethanol case for comparison with experiments.

Our propagation model is based on the nonlinear Schrödinger (NLS) equation for the electric field envelope $\mathcal{E}(x, y, z, t)$ moving with the group velocity of the input laser beam,

$$\frac{\partial}{\partial z}\mathcal{E} = \frac{i}{2k}\left(\frac{\partial^2}{\partial x^2} + \frac{\partial^2}{\partial y^2}\right)\mathcal{E} - i\frac{k''}{2}\frac{\partial^2}{\partial t^2}\mathcal{E} + ik_0 n_2|\mathcal{E}|^2\mathcal{E} - \left(\frac{ik_0}{2n_0\varrho_c} + \frac{\sigma}{2}\right)\varrho\mathcal{E} - \frac{\beta^{(K)}}{2}|\mathcal{E}|^{2K-2}\mathcal{E}\,, \quad (1)$$

$$\frac{\partial}{\partial t}\varrho = \sigma_K \varrho_{\rm nt}|\mathcal{E}|^{2K} + \frac{\sigma}{U_i}\varrho|\mathcal{E}|^2 - \frac{\varrho}{\tau_{\rm r}}\,, \quad (2)$$

where z is the propagation distance and t stands for the retarded time. On the right-hand side of (1), the central wavenumber is defined by $k = n_0 k_0$ for $k_0 = 2\pi/\lambda_0$, $\lambda_0 = 810\,{\rm nm}$ and the linear refractive index $n_0 = 1.36$ for pure ethanol. The first term describes spatial diffraction, while the second one accounts for group-velocity dispersion (GVD) with coefficient $k'' \simeq 403\,{\rm fs}^2/{\rm cm}$ [33]. The third contribution refers to the Kerr response, taken as instantaneous with the nonlinear index $n_2 = 2.6 \times 10^{-16}\,{\rm cm}^2/{\rm W}$ for ethanol [34]. The critical power for self-focusing is thus about 3 MW. The next three terms correspond to plasma gain and losses, including multiphoton absorption with $\beta^{(K=6)} = 8.53 \times 10^{-65}\,{\rm cm}^9/{\rm W}^5$, from ionization of ethanol molecules. The source equation (2) accounts for plasma formation by multiphoton ionization, avalanche ionization, and electron recombination over long time scales, $\tau_{\rm r} = 450\,{\rm ps}$ [35]. Electron transitions to the conduction band take place with the gap potential $U_i = 8.4\,{\rm eV}$, yielding six-photons transitions ($K = 6$) at 810 nm [36] with the multiphoton cross-section $\sigma_{K=6} = 5.63 \times 10^{-69}\,{\rm s}^{-1}\,{\rm cm}^{12}/{\rm W}^6$ [37] and the neutral density $\varrho_{\rm nt} = 1.03 \times 10^{22}\,{\rm cm}^{-3}$, critical plasma density $\varrho_{\rm c} =$

$1.7 \times 10^{21}\,\mathrm{cm}^{-3}$, and inverse bremstrahlung cross-section $\sigma = 1.22 \times 10^{-17}\,\mathrm{cm}^2$. It should be noted that we neglect space-time focusing, self-steepening and dispersion of higher than second order, as they are not critical for the present arrangements of small-scale filamentation [20]. In particular, our FWHM pulse duration ($\tau = 120\,\mathrm{fs}$) implies that the product $\omega_0\tau \gg 1$ is less critical compared to the pulses used in [20, 21].

We simulate three major classes of input beam shape, corresponding to different diffractive elements in the beam path, namely, no element, a circular aperture, and a slit. A slit, rather than a sharp edge, is simulated as the third type of element for computational ease; only that portion of the numerical results in the vicinity of one sharp edge should be compared to the experimental case. For each input shape, we fix the initial intensity at approximately the measured value $\left(I_0^{\max} = 4 \times 10^{11}\,\mathrm{W/cm}^2\right)$, while also keeping the values of spot size w_0 and input power P_{in} comparable to those employed in the experiments. Each beam is modeled as a Gaussian in the temporal domain, with $t_{\mathrm{p}} = 102\,\mathrm{fs}$ (120 fs FWHM). For the open beam (no diffractive element) we assume a Gaussian spatial profile, perturbed by random noise of 15% relative amplitude

$$\mathcal{E}(x, y, t, z = 0) = \sqrt{\frac{2P_{\mathrm{in}}}{\pi w_0^2}} \times (1 + 0.15 \times \mathrm{noise}) \times \mathrm{e}^{-\frac{x^2+y^2}{w_0^2} - \frac{t^2}{t_p^2}}, \tag{3}$$

where $w_0 = 1\,\mathrm{mm}$ and $P_{\mathrm{in}} \simeq 6.3\,\mathrm{GW}$. To simulate the beam profile after a circular aperture, we choose a super-Gaussian in space

$$\mathcal{E}(x, y, t, z = 0) = \sqrt{\frac{2^{\frac{1}{N}} P_{\mathrm{in}}}{\Gamma\left(1 + \frac{1}{N}\right) \pi w_0^2}} \times (1 + 0.15 \times \mathrm{noise}) \times \mathrm{e}^{-\left(\frac{x^2+y^2}{w_0^2}\right)^N - \frac{t^2}{t_p^2}}, \tag{4}$$

where $w_0 = 0.5\,\mathrm{mm}$ and $P_{\mathrm{in}} \simeq 2.8\,\mathrm{GW}$. Choosing $N = 10$ gives a peak input intensity of $I_0^{\max} = 4 \times 10^{11}\,\mathrm{W/cm}^2$, close to the experimental value of $I_0 \gtrsim 3 \times 10^{11}\,\mathrm{W/cm}^2$.

Finally, we model the beam entering the slit configuration with an asymmetric super-Gaussian profile for the spatial distribution of the field envelope

$$\mathcal{E}(x, y, t, z = 0) = \sqrt{\frac{2^{\frac{1}{2N}-2} P_{\mathrm{in}}}{\sqrt{\frac{\pi}{2}}\Gamma\left(1 + \frac{1}{2N}\right) w_0^2}} \times (1 + 0.15 \times \mathrm{noise}) \times \mathrm{e}^{-\left(\frac{x^2}{w_0^2}\right)^N - \frac{y^2}{4w_0^2} - \frac{t^2}{t_p^2}}, \tag{5}$$

with $w_0 = 0.5\,\mathrm{mm}$, $N = 10$, $P_{\mathrm{in}} \simeq 4.7\,\mathrm{GW}$ and the same peak input intensity as above.

The simulations require high spatial resolution in order to represent the multifilamentation process accurately; each filament has a diameter on the order of a ten of microns. Hence, a spatial mesh size of 2 μm was employed, while pulse shortening induced by plasma defocusing imposed a temporal step size close to 1 fs. We performed three different computations in pure ethanol, presented in Fig. 5, to simulate the influence of the diffractive elements on the output fluence distributions in the transverse plane. Parts (a) and (b) of Fig. 5 should be compared with their experimental counterparts (Fig. 3a and b), recalling that we only expect qualitative resemblance due to the cleanness of the spatial profile input to the numerical model. Part (c) displays filaments formed from both edges of the slit. This reproduces the experimental behavior of Fig. 3c, neglecting the right-hand half of the numerical results.

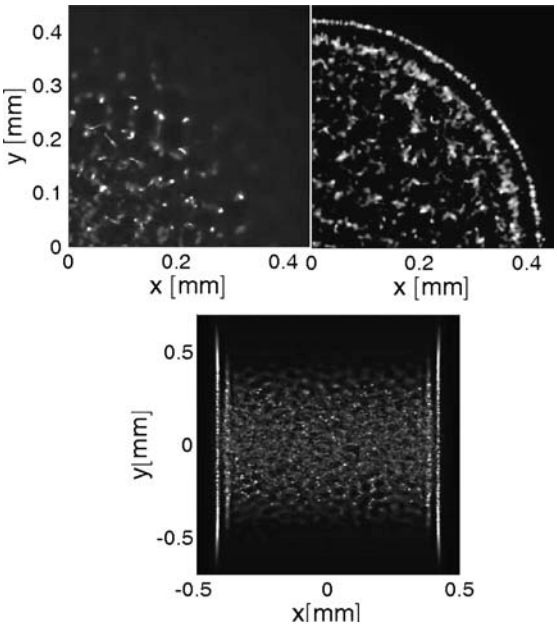

FIGURE 5 Calculated fluence profiles at the cell exit for filament formation in pure ethanol. Comparison of the effect of various diffractive elements: (**a**) no diffractive element; (**b**) circular aperture; (**c**) vertical slit (two sharp edges)

3.3 *Comparison between experiments and simulations*

Numerical results are in good qualitative agreement with those resulting from experiments in regard to the major features outlined above. We retrieve the diffraction-induced rings (for the circular aperture) and stripes (for the sharp edge), compared with the random-seeming arrangement of filaments when no diffractive element is present. The sharp intensity gradients formed in the transverse plane are again seen to overwhelm other wavefront instabilities, with the first (and most intense) filaments forming along the outermost diffraction maxima. As the beam propagates, the requisite intensity and intensity-gradient conditions are met along successive (from the outside towards the center) maxima, leading to the development of small-scale filaments in these regions. This process provides a framework for filament nucleation which is absent in Fig. 5a, where a lower filament density is observed after the same propagation distance (1 cm), compared to Fig. 5b. As in the experimental

case, this framework also implies constant inter-filament distances. The good agreement between experiment and simulation regarding the major features of filament control (pattern and inter-filament distance) validates the concept of employing diffractive elements for control purposes. There remain, however, other output parameters, such as filament number and intensity, which also depend strongly on the competing processes involved in filament propagation. One of these, namely the TPA losses, is examined in the following section.

4 Effect of dye concentration on filament creation

In this section, we discuss the influence of TPA losses on filament formation, as probed by a varying coumarin concentration. We first summarize briefly our previous numerical results on the differences between filament propagation through ethanol and through a solution of coumarin 153 in ethanol, as presented in [16]. In contrast to investigations on methanol [21], which followed the evolution of individual filaments, our former computations examined the maximum intensity and electron density over both the spatial wavefront enclosing many filaments and the pulse duration. In the case of pure ethanol, a dynamic balance between optical self-focusing and plasma generation led to self-channeling beyond the nonlinear focal point. Such a dynamic process was not, however, observed for the high-concentration coumarin solution ($C = 4$ g/l). In this case, we observed the filaments to have a somewhat larger diameter (15–20 μm compared to 8–10 μm) than those in pure ethanol. Moreover, beam collapse (tracked by the nonlinear focal point) was arrested at lower core intensity values by TPA losses [16], causing fewer filaments to emerge. The latter result is the most prominent feature evident in Fig. 6, in which the output fluence distribution is compared for a range of coumarin concentrations from 0.7 to 2.8 g/l. In other words, the higher the concentration, the greater the TPA losses, and thus the fewer the filaments created. The predicted relationship between concentration and filament diameter, however, does not materialize in our experimental data, as presented in Fig. 6. This is because we chose to image a large field of view in order to track variation in filament patterns, meaning that the resolution is insufficient to measure differences in filament diameter precisely.

As identical camera parameters were employed for all images in Fig. 6, the saturation present in Fig. 6c suggests that filaments increase in intensity as the dye concentration is decreased. This result is hardly surprising, as reducing the coumarin concentration means that less energy is lost through TPA, such that filament formation is arrested at higher intensities. Finally, comparing the different images in Fig. 6, we see that, although fewer filaments are formed at higher concentrations, the position of individual filaments remains stable. That is, increasing the losses from TPA only "turns off" some filament sites, depending on the intensity available, as was also seen in Fig. 4. Recalling that this set of experiments was performed with the same circular aperture in place, it is clear that filament-pattern control using diffractive elements is effective over a range of dye concentrations, resulting in highly repeatable filament positions. This stability and control is exploited in the following investigation to produce repeatable arrays of lasing sources.

5 Filament-generated lasing sources

In this set of experiments, the control properties discussed above are harnessed to produce highly reproducible arrays of ~ 10 μm-size sources of laser radiation. While in [16] we compared amplified spontaneous emission (ASE) through filaments to stimulate emission initiated by a dump pulse, we now present results showing the control of lasing arrays using a sharp edge.

Results in this section correspond to the output filament pattern for a beam encountering a sharp edge (see Fig. 3c). Adding the 530 nm dump pulse transforms each filament site seen in that figure into a lasing source, with TPA from filaments providing a means of pumping the nonlinear medium. Clearly, two-photon excitation is much more efficient along the filament sites, due to their higher intensity compared to that of the surrounding beam. While TPA occurs in a band around 420 nm, coumarin 153 fluoresces around 530 nm. As a result, photons at the latter wavelength incident on the nonlinear medium initiate a stimulated emission, or lasing pro-

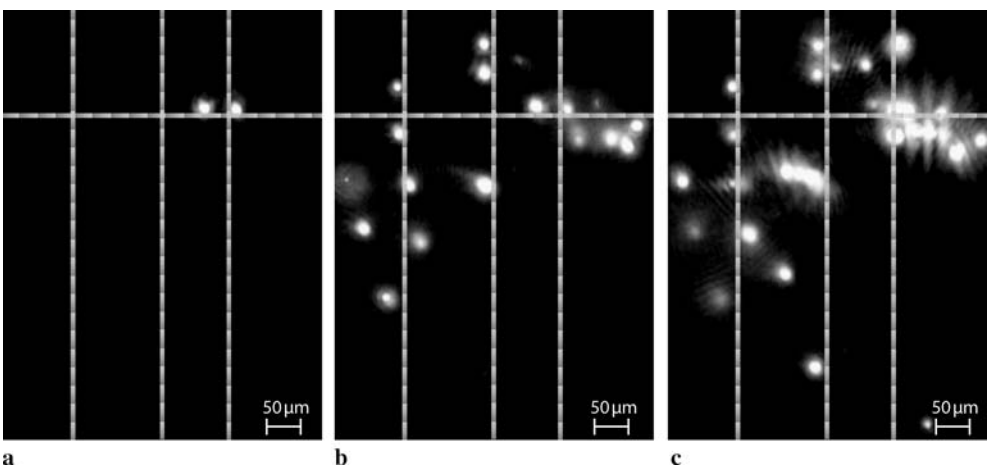

FIGURE 6 Output fluence distributions for a range of coumarin 153 concentrations (in ethanol): (**a**) $C = 2.8$ g/l; (**b**) $C = 1.3$ g/l; (**c**) $C = 0.7$ g/l. Note that all *images* were acquired using identical camera parameters, such that *image* (**c**) is saturated. Grid is for comparison purposes

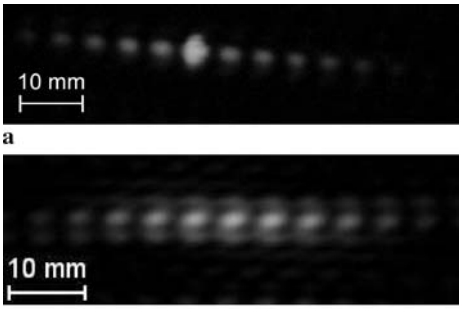

FIGURE 7 A typical set of results for the lasing filaments experiment. *Images* correspond to pump and dump pulses having encountered a sharp edge: (**a**) far-field interference pattern at 530 nm, corresponding to filaments in Fig. 3c; (**b**) Fourier transform of filament sites in Fig. 3c

cess. The much higher concentration of excited dye molecules along the filament sites privileges laser action along these "gain channels". In other words, a set of localized lasing sources is produced. Furthermore, these sources are seen to be coherent with one another. In order to verify both these properties, localization and coherence, we image the resultant far-field interference pattern at 530 nm. The far-field image corresponding to the lasing filaments of Fig. 3c is presented in Fig. 7a. This evidently resembles a Young's double slit interference pattern, with the high contrast between bright and dark fringes attesting the coherence of the originating filament sources. It should be noted that this coherence follows from that of the dump pulse, and not from coherence between individual filaments, as demonstrated in [38]. Although the double "stripe" arrangement of filaments strongly suggests that they are responsible for the far-field pattern, we further check this issue by performing simple calculations for double-slit interference. The separation of interference maxima in the far-field is measured to be around 5 mm. This should correspond to a distance between "slits" of $\lambda D/d \approx 210\,\mu$m, where $\lambda = 530$ nm, $D = 2$ m (from the cell output to the far-field imaging location), and d is the distance between maxima. This agrees closely with the approximately 200 μm distance between filament "stripes". Furthermore, the far-field pattern's overall extent (about 50 mm) may be linked to the characteristic filament size (20 μm). A final proof is afforded by taking a Fourier transform of the output filament pattern; this must be equivalent to the far-field interference result. Comparing the Fourier transform image (Fig. 7b) with the far-field pattern (Fig. 7a), this equivalence is clearly present. The arrays of filaments seen in Fig. 3c are thus demonstrated to be localized, coherent lasing sources. The only significant difference between Fig. 7a and b lies in the size of the central spot, which is larger in the experimental image, reflecting the fact that the lasing sources are not perfectly coherent.

The ability to control the distribution of this lasing array depends not only on the vertical "stripe" pattern produced, but also on its stability from shot to shot. The far-field pattern in Fig. 7a was acquired as the sum of at least 200 individual laser shots. If the position of the lasing filaments varied between shots, the far-field image would not show such high contrast between bright and dark maxima. It is clear, therefore, that filament-pattern control using diffractive elements may be applied to manipulate arrays of lasing sources.

6 Conclusion

We have confirmed that it is possible to control the pattern of filaments generated in a nonlinear absorbing medium by placing a diffractive element in the input beam path. The nonlinear medium under consideration was a high-concentration dye solution (coumarin 153 in ethanol), which is of interest because concentrated solutions, resulting in high TPA, have been rarely studied so far. For a range of diffractive elements (circular aperture, sharp edge), intensity gradients resulting from beam diffraction were seen to swamp random fluctuations on the wavefront, forcing filament nucleation along diffraction maxima. These results were in close agreement with numerical simulations. The filament patterns created are highly repeatable, with filament number able to be modified in a deterministic way by varying the dye concentration. Stability and reproducible-pattern features were finally exploited to create controllable arrays of lasing filaments, with laser action occurring along gain channels produced by strong TPA at the filament sites. Such tens-of-micrometer localized lasing sources foreshadow innovative laser devices, which may be exploited for further applications.

REFERENCES

1 L. Bergé, S. Skupin, R. Nuter, J. Kasparian, J.P. Wolf, Rep. Prog. Phys. **70**, 1633 (2007)
2 S.L. Chin, S.A. Hosseini, W. Liu, Q. Luo, F. Theberge, N. Akozbek, A. Becker, V.P. Kandidov, O.G. Kosareva, H. Schroeder, Can. J. Phys. **83**, 863 (2005)
3 A. Couairon, A. Mysyrowicz, Phys. Rep. **441**, 47 (2007)
4 V.I. Bespalov, V.I. Talanov, JETP Lett. **3**, 307 (1966)
5 A.J. Campillo, S.L. Shapiro, B.R. Suydam, Appl. Phys. Lett. **23**, 628 (1973)
6 L. Bergé, C. Gouédard, J. Schjødt-Eriksen, H. Ward, Physica D **176**, 181 (2003)
7 J. Meier, G.I. Stegeman, D.N. Christodoulides, Y. Silberberg, R. Morandotti, H. Yang, G. Salamo, M. Sorel, J.S. Aitchison, Phys. Rev. Lett. **92**, 163 902 (2004)
8 V.P. Kandidov, N. Akozbek, M. Scalora, O.G. Kosareva, A.V. Nyakk, Q. Luo, S.A. Hosseini, S.L. Chin, Appl. Phys. B **80**, 267 (2005)
9 H. Schroeder, J. Liu, S.L. Chin, Opt. Express **12**, 4768 (2004)
10 Z. Hao, J. Zhang, Z. Zhang, X. Yuan, Z. Zheng, X. Lu, Z. Jin, Z. Wang, J. Zhong, Y. Liu, Phys. Rev. E **74**, 066 402 (2006)
11 Z. Hao, J. Zhang, X. Lu, T.-T. Xi, Y.-T. Li, X.-H. Yuan, Z.-Y. Zheng, Z.-H. Wang, W.-J. Ling, Z.-Y. Wei, Opt. Express **14**, 773 (2006)
12 A. Dubietis, G. Tamosauskas, G. Fibich, B. Ilan, Opt. Lett. **29**, 1126 (2004)
13 G. Méchain, A. Couairon, M. Franco, B. Prade, A. Mysyrowicz, Phys. Rev. Lett. **93**, 035 003 (2004)
14 K. Cook, R. McGeorge, A.K. Kar, M.R. Taghizadeh, R.A. Lamb, Appl. Phys. Lett. **86**, 021 105 (2005)
15 G. Heck, J. Sloss, R.J. Levis, Opt. Commun. **259**, 216 (2006)
16 L. Guyon, F. Courvoisier, V. Boutou, R. Nuter, A. Vinçotte, S. Champeaux, L. Bergé, P. Glorieux, J.-P. Wolf, Phys. Rev. A **73**, 051 802 (2006)
17 J. Kasparian, M. Rodriguez, G. Mejean, J. Yu, E. Salmon, H. Wille, R. Bourayou, S. Frey, Y.B. Andre, A. Mysyrowicz, R. Sauerbrey, J.-P. Wolf, L. Woste, Science **301**, 61 (2003)
18 M. Kolesik, E.M. Wright, J.V. Moloney, Phys. Rev. Lett. **92**, 253 901 (2004)
19 A. Dubietis, E. Gaizauskas, G. Tamosauskas, P. Di Trapani, Phys. Rev. Lett. **92**, 253 903 (2004)
20 W. Liu, S.L. Chin, O. Kosareva, I.S. Golubtsov, V.P. Kandidov, Opt. Commun. **225**, 193 (2003)
21 H. Schroeder, S.L. Chin, Opt. Commun. **234**, 399 (2004)
22 S. Skupin, R. Nuter, L. Bergé, Phys. Rev. A **74**, 043 813 (2006)
23 C. D'Amico, B. Prade, M. Franco, A. Mysyrowicz, Appl. Phys. B **85**, 49 (2006)
24 G.S. He, R. Signorini, P.N. Prasad, Appl. Opt. **37**, 5720 (1998)

25 Q. Luo, W. Liu, S.L. Chin, Appl. Phys. B **76**, 337 (2003)
26 F. Théberge, N. Aközbek, W. Liu, A. Becker, S.L. Chin, Phys. Rev. Lett. **97**, 023 904 (2006)
27 R. Weigand, M. Wittmann, J.M. Guerra, Appl. Phys. B **73**, 201 (2001)
28 W.J. Firth, A.J. Scroggie, Phys. Rev. Lett. **76**, 1623 (1996)
29 M.D. Feit, J.A. Fleck, J. Opt. Soc. Am. B **5**, 633 (1988)
30 A. Vinçotte, L. Bergé, Physica D **223**, 163 (2006)
31 M. Mlejnek, M. Kolesik, J.V. Moloney, E.M. Wright, Phys. Rev. Lett. **83**, 2938 (1999)
32 M. Kolesik, J.V. Moloney, Opt. Lett. **29**, 590 (2003)
33 J. Rheims, J. Köser, T. Wriedt, Meas. Sci. Technol. **8**, 601 (1997)
34 Q.H. Gong, J.L. Li, T.Q. Zhang, H. Yang, Chin. Phys. Lett. **15**, 30 (1998)
35 Q. Feng, J.V. Moloney, A.C. Newell, E.M. Wright, K. Cook, P.K. Kennedy, D.X. Hammer, B.A. Rockwell, C.R. Thompson, IEEE J. Quantum Electron. **QE-33**, 127 (1997)
36 J.M. Jung, H. Gress, Chem. Phys. Lett. **359**, 153 (2002); J.M. Jung, Chem. Phys. Lett. **366**, 67 (2002)
37 L.V. Keldysh, Sov. Phys. JETP **20**, 1307 (1965)
38 W. Watanabe, K. Itoh, Japan. J. Appl. Phys. **40**, 592 (2001)